




Experimental study of a drill string test rig and the construction of torsional stability maps

A. D. dos Santos¹ · A. T. Fleury¹ · A. L. D. da Costa² · T. G. Ritto² 

Received: 8 August 2024 / Accepted: 15 February 2025 / Published online: 1 March 2025

© The Author(s), under exclusive licence to The Brazilian Society of Mechanical Sciences and Engineering 2025

Abstract

Slender shafts subjected to local friction have important applications, such as in drilling. Also, stability maps are important tools that guide decision makers. These stability maps are affected by initial conditions, boundary conditions, and so on. Although used abundantly, there are few articles that investigate their sensitivity with respect to initial conditions. Moreover, there is no experimental attempt in this sense, up to the authors' knowledge. The main contribution of this paper is to propose a methodology to construct, experimentally, torsional stability maps for different conditions: (i) starting the system with friction contact from rest, (ii) starting with rotation before the friction contact, and (iii) imposing axial oscillation of the platform. These conditions are important to be analyzed, because they might happen in a real drill string system. The findings indicate that initiating shaft rotation prior to axial contact and applying axial oscillations during contact contribute to improving torsional stability. In addition, depending on some conditions (e.g., temperature and material wear), the results change considerably. The experimental results obtained here might guide other developments, including new stochastic models to take into account uncertainties.

Keywords Drill string dynamics · Laboratory test rig · Experiment analysis · Nonlinear dynamics · Stability map

1 Introduction

The drilling process is vital in the oil and gas industry as it allows for the exploration, extraction, and production of valuable energy resources. By creating boreholes, drilling

enables access to underground reservoirs of oil and gas, providing essential energy sources for transportation, electricity, and heating.

Drill string dynamic behavior is an active topic of research. Some researchers are interested in the modeling aspects [1–5], others in control [6–9], others in uncertainties [10–12].

The present paper is interested in drill string dynamics [1, 13, 14], and a test rig is an important tool for studying this nonlinear dynamic system [15, 16]. It allows engineers to analyze the behavior of the system under various conditions, even though the laboratory experiment is not a scaled version of the real system. As mentioned in [16], the reduction in diameter would be no longer achievable if one tries to mimic a long drill string. Therefore, the goal here (and of other drilling test rigs) is to have an experiment that helps us understand some important phenomena that happen in the real system. This analysis provides some insights for the application of interest.

Patil et al. [15] presented laboratory test rigs built to reproduce some vibration modes, with emphasis on torsional dynamics. More recently, Srivastava et al. [16] did an extensive review of laboratory experimental setups for

Technical Editor: Adriano Todorovic Fabro.

✉ T. G. Ritto
tritto@mecanica.ufrj.br

A. D. dos Santos
adrianodomeny@alumni.usp.br

A. T. Fleury
agenorfleury@usp.br

A. L. D. da Costa
andreluisdutra@poli.ufrj.br

¹ Department of Mechanical Engineering, Escola Politécnica da Universidade de São Paulo, Av. Prof. Mello Moraes, 2231, Engenharia Mecânica, Sala TT-11 térreo, São Paulo, SP 05508-030, Brazil

² Department of Mechanical Engineering, Universidade Federal do Rio de Janeiro - UFRJ, Cidade Universitária, Centro de Tecnologia, bloco G, Sala 202, Rio de Janeiro, RJ 21945-970, Brazil

studying drill string vibrations. Next, we will comment on some laboratory test rigs.

Liao et al. [17] analyzed a torsional–lateral rig, where lateral contact between a disk and a fixed ring is considered. Mihajlovic et al. [18] studied the influence of friction characteristics on limit cycling in torsional dynamics and how friction characteristics depend on temperature and normal forces. The setup consists of two disks, a low-stiffness string, and an additional brake applied to the lower disk. Cayres et al. [19] also investigated the torsional vibration underlying stick–slip oscillations originating from dry friction at rotor–stator contact. The torsional test rig consists of a horizontal slender shaft where an electric motor drives two disks. Friction is induced by two braking systems.

Real et al. [20] analyzed the axial–torsional coupled dynamics considering real drilling with a masonry bit. The test rig was able to satisfactorily represent some phenomena observed in deep water drilling, such as stick–slip oscillations and hysteric cycles [21]. Kapitaniak et al. [22] constructed a rig that might use commercial drill bits and rock samples, and dynamic investigations, such as stick–slip oscillations, whirling, drill bit bounce, and helical buckling can be performed. We can also find other recent experimental investigations related to the drill string dynamics in [23–27].

This paper presents a test rig built at the *Universidade de São Paulo* (USP) to study drill string dynamic phenomena and is able to evaluate lateral, torsional, and axial dynamics. The vertical rig is composed of a slender shaft and two disks, one at the bottom and the other at an intermediate position. A servomotor rotates the system from the top, and a stepper motor can move the shaft longitudinally. At the bottom, pins are used to introduce friction and emulate the bit–rock interaction. The test bench is more detailed in [28, 29].

The main contribution of this paper is to propose a methodology to construct, experimentally, torsional stability maps for different conditions: (i) starting the system with friction contact from rest, (ii) starting with rotation before friction contact, and (iii) imposing axial oscillation of the platform. This investigation has not been attempted by any of the previous works, to the best of the authors' knowledge, and the conditions considered are important to be analyzed because they might happen in a real drill string system.

The paper is organized as follows. The test rig is presented in Sect. 2. Section 3 gives some theoretical considerations, and Sect. 4 shows the experimental time responses. Finally, the methodology to construct the experimental stability maps is presented in Sect. 5, and the experimental stability maps are analyzed for different operational conditions in Sect. 6. Concluding remarks are made in the last section.

2 Test rig

The test rig presented in this paper was developed at the *Universidade de São Paulo*. It is an improvement in previous works developed by the authors. In [30], the torsional dynamic behavior of a test bench composed of a DC motor coupled to a shaft, subjected to frictional forces that induce stick–slip, is analyzed. In [31], the sliding mode control is implemented to stabilize the angular velocity of a slim and flexible rotary system subjected to dry friction. In [32], the sliding mode control is used to stabilize the orbit of a rotor, subjected to lateral impact and rubbing, through shaft traction actuation.

The present test rig is equipped with a slender metallic axis (main axis), positioned vertically, and supported at its upper end on a mobile platform, with freedom for vertical movement. Two massive rotors are attached to the main shaft: one at its lower end (main rotor) and another in an intermediate position (intermediate rotor). The main rotor is important to increase the inertia of the system at the bottom and highlight the torsional oscillations. The intermediate rotor will be important for future investigations, where lateral impacts might happen. In the present paper, we are interested in the torsional dynamics; hence, the added inertia from the intermediate rotor increases the inertia of the system and does not compromise the current analysis.

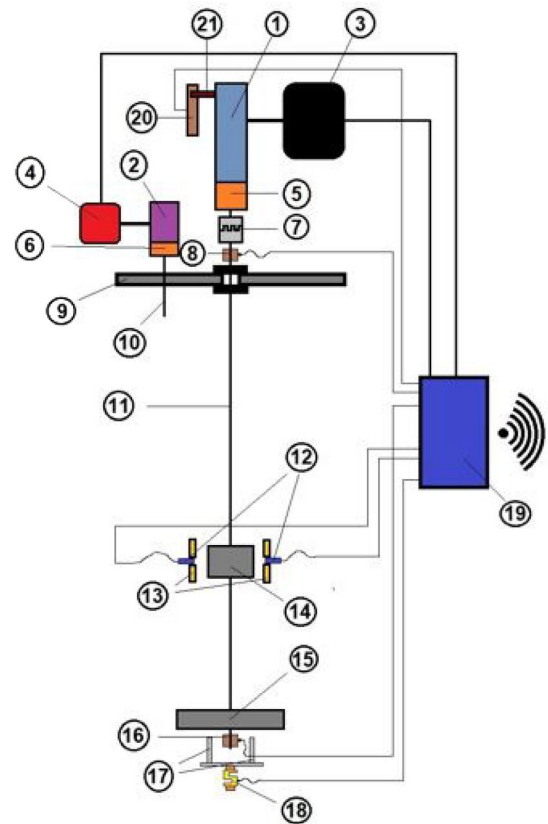
Figure 1 shows a picture of the prototype, and Fig. 2 sketches the experimental setup. Table 1 lists some of its dimensions, and Table 2 lists the material properties.



Fig. 1 Test bench prototype

Fig. 2 Test bench schematic

1. Servo motor
2. Stepper motor
3. Servo driver
4. Stepper motor driver
5. Servo reducer
6. Stepper motor reducer
7. Coupling
8. Upper encoder
9. Mobile platform
10. Spindle axis
11. Main axis
12. Distance sensors
13. Cylindrical shell
14. Intermediate rotor
15. Main rotor
16. Lower encoder
17. Friction pins
18. Load cell (normal force)
19. Data acquisition device
20. Load cell (reaction torque)
21. Lever arm

**Table 1** Test bench geometry

Description	Symbol	Measure (mm)
Total height	–	3500
Width	–	600
Depth	–	600
Main shaft length	L	2500
Main shaft diameter	d	3
Distance between motor and intermediate rotor	L_1	2000
Intermediate rotor diameter	D_{r_2}	140
Intermediate rotor thickness	\bar{L}_2	60
Main rotor diameter	D_{r_1}	250
Main rotor thickness	\bar{L}_1	30

Table 2 Test bench material

Material property	Symbol	Value (mm)
Density	ρ	$7.85 \times 10^3 \text{ kg/m}^3$
Poisson coefficient	ν	0.3
Elasticity modulus	E	$200 \times 10^9 \text{ Pa}$
Shear modulus	G	$76.9 \times 10^9 \text{ Pa}$

Ideally, a test bench should be similar to the system of interest [16, 33]. However, as stated in [16] “If one were to choose an aggressive scaling factor for mimicking a longer section for accuracy, the reduction in diameter would be no longer achievable.” Therefore, the goal here (and of other drilling test rigs) is to have an experiment that helps us understand some important phenomena that happen in the real system. This analysis provides some insights for the application of interest. If we consider the data from [1], we have the following downscaling factors: ratio of the length of test rig shaft to the length of real drill pipe $2.5/1,400 = 0.002$, ratio of the diameters $0.0030/0.2286 = 0.01$, ratio of the imposed speeds $50/100 = 0.5$, and ratio of the normal forces $50/100,000 = 0.0005$.

The axial displacement of the platform δ , and, consequently, of all the other mobile components of the workbench, is carried out by the actuation of a stepper motor. The maximum vertical displacement of the platform is 2mm, with an accuracy of 5×10^{-4} mm. In addition, the main shaft is connected to a servomotor at the top, which imposes a nominal speed of rotation. Finally, two pins are placed at the bottom to introduce friction and emulate the bit–rock interaction. The applied nonlinear interaction in the experiment, although different, has a similar effect in creating torsional resistance. As a consequence, it is possible to observe

torsional stick–slip oscillations in experiments [19, 20], field data [35, 36], and numerical simulations [34].

The bench is instrumented with a total of seven sensors: two load cells, one for measuring the reaction torque on the servomotor and another for measuring the normal contact force between the main disk and the friction pins; two encoders, for estimating the rotation speed of the main disk and the output of the servo motor; and three proximity sensors to estimate the lateral orbit of the intermediate rotor.

3 Theoretical considerations

Before analyzing the experimental responses, a simple torsional model is considered to serve as a guideline for what to expect from our experiment, if torsional vibrations are dominant [12, 34]:

$$I_{eq}\ddot{\theta}(t) + c_{eq}\dot{\theta}(t) + k_{eq}\theta(t) = k_{eq}\Omega t + c_{eq}\Omega - T_{bit}(\dot{\theta}(t)), \quad (1)$$

where $\theta(t)$ is the angular velocity at the bottom, I_{eq} , c_{eq} , k_{eq} are the equivalent inertia, damping, and stiffness of the system, and Ω is the imposed angular speed at the top. Rewriting Eq. 1, now including the expression of nonlinear torque on bit $T_{bit}(\dot{\theta}(t))$ [37, 38]:

$$\ddot{\theta}(t) + 2\xi\omega_n\dot{\theta}(t) + \omega_n^2\theta(t) = \omega_n^2\Omega t + 2\xi\omega_n\Omega - b_n\left(\tanh(b_1\dot{\theta}) + \frac{b_2\dot{\theta}}{(1+b_3\dot{\theta}^2)}\right), \quad (2)$$

where $\xi = c_{eq}/(2\sqrt{I_{eq}k_{eq}})$ is the damping ratio, $\omega_n = \sqrt{k_{eq}/I_{eq}}$ is the natural frequency, b_n is a constant normalized by I_{eq} , which is related to the normal force and friction coefficient, and b_1 , b_2 , b_3 are the parameters of the nonlinear interaction model at the bottom.

It has been shown [12, 34] that, although simple, this model is able to well represent torsional oscillations and linearized stability maps. Of course, it is not able to capture the dynamics associated with higher frequencies. The real system is more complex, and further development is needed considering a more complete model (finite element, etc.) and uncertainties, which is out of the scope of this paper.

4 Experimental time response

This section details the dynamic responses obtained for the rotational speed of the main rotor. First, the free response is analyzed; see Fig. 3. It indicates that the first torsional natural frequency is about 0.275 Hz and the corresponding damping rate is about 5%. In this procedure,

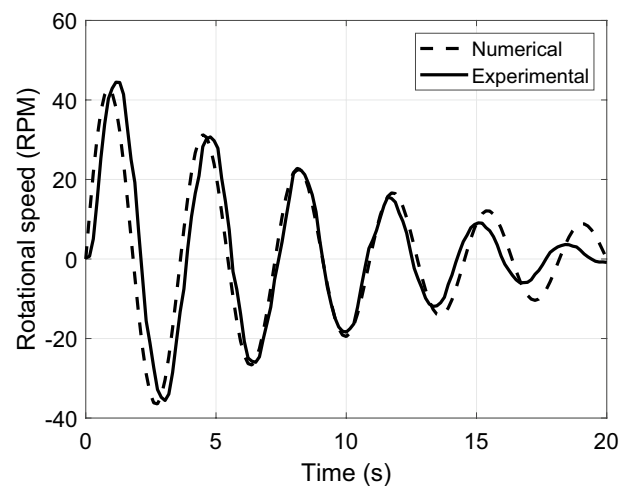


Fig. 3 Free response of the main rotor (rotational speed vs. time). Experimental response in continuous line and numerical response in dashed line

friction is imposed on the main rotor (through the pins) to lock it, while a rotation is imposed at the top. Then, the pins are detached from the rotor zeroing the friction and allowing the system to oscillate freely. It is observed (Fig. 3) that the numerical response is close to the experimental one. The simplified model represents qualitatively the free response of the analyzed system, although some discrepancy is observed due to the simplified hypotheses. The numerical response is obtained using the analytical solution of a free damped oscillator: $x_{num} = (\dot{\theta}_0/\omega_d)\exp(-\xi\omega_n t)\sin(\omega_d t)$, where $\omega_d = 0.275 \times 2\pi$ rad/s, $\omega_n = \omega_d/\sqrt{(1-\xi^2)}$, $\xi = 0.05$, and $\dot{\theta}_0 = 80$ rad/s.

Figure 4 illustrates the typical rotational speed signals for different dynamic behaviors of the system. In Fig. 4a, the rotational speed signal is characterized by an intermittent sequence of stick–slip oscillations with frequency of about 0.15 Hz (nearly half of the natural frequency of 0.27 Hz). Note that, in the specific case of $\Omega_{ref} = 5$ RPM and $\delta = 0.4$ mm, the lowest speed peak exceeds three times the nominal speed value, and the highest peak almost reaches six times this value.

In Fig. 4b, the rotational speed signal is characterized by a permanent regime with high torsional oscillations and a given modulation. The higher frequency is about 0.26 Hz (a little lower than the natural frequency), and the modulation frequency is about 0.03 Hz. This dynamic regime is called transition zone type 2 (see next section).

In Fig. 4c, the rotation speed signal is characterized by an onset of stick–slip oscillations, followed by small oscillations around the reference speed at the top. It is important to emphasize that even if there is a stall at the beginning, it is necessary to wait to verify if the stick–slip

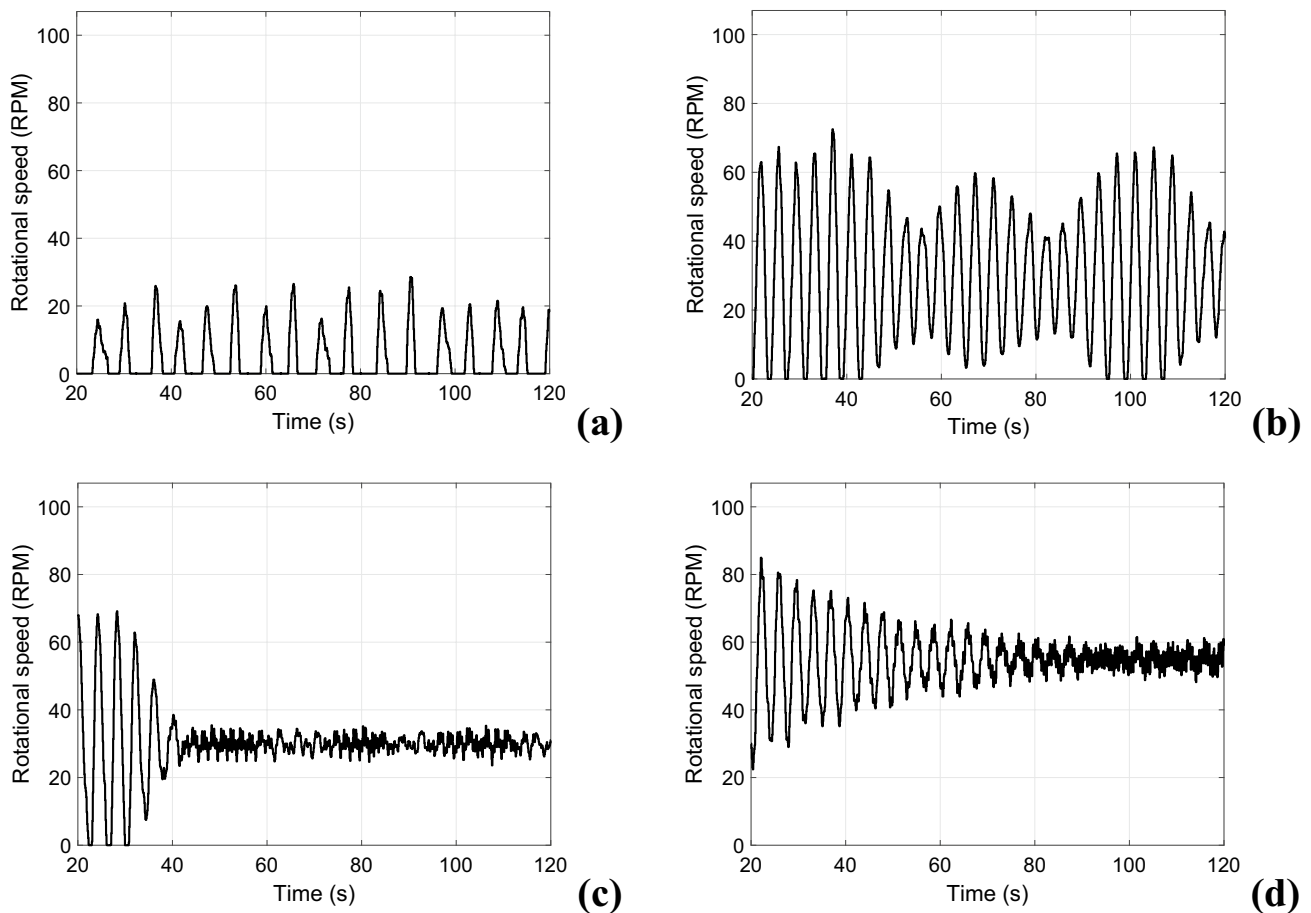


Fig. 4 Typical experimental rotational speed signals over time. **a** $\Omega_{\text{ref}} = 5$ RPM, $\delta = 0.4$ mm. The stick-slip frequency is about 0.15 Hz. **b** $\Omega_{\text{ref}} = 30$ RPM, $\delta = 0.35$ mm. The high frequency is about

0.26 Hz and the modulation frequency about 0.03 Hz. **c** $\Omega_{\text{ref}} = 30$ RPM, $\delta = 0.6$ mm. **d** $\Omega_{\text{ref}} = 55$ RPM, $\delta = 0.45$ mm

oscillations will prevail. This dynamic regime is called transition zone type 1 (see next section).

Finally, in Fig. 4d, the rotational speed is characterized by the absence of any type of locking throughout the test time. After about 80 s of transient, the steady state is achieved. The steady state presents some oscillations which might be associated with disturbance, and lateral and torsional frequencies.

Figure 5 shows the rotational speed model response for two conditions (imposed speed and parameter b_n). The parameter b_n is related to the normal force and friction coefficient. As mentioned in the previous section, the model is able to represent responses with and without torsional oscillations, but it cannot reproduce higher frequencies. The black line shows a stable response and the red line an unstable one. However, the variety of responses observed in the experiment is greater than the one reproduced by the model, as expected. The following bit-rock interaction model parameter values were used: $b_1 = 0.4775$, $b_2 = 8.7854$, $b_3 = 2.2797$. The nonlinear equation was numerically solved

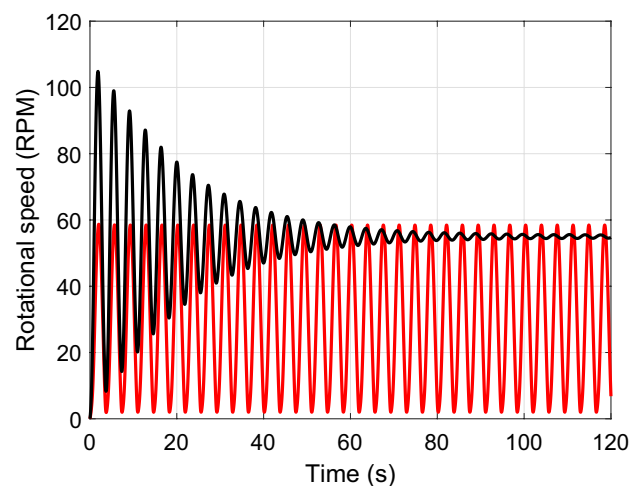


Fig. 5 Rotational speed obtained by the numerical model considering stable (black line) and unstable (red line) conditions. Black line: $\Omega_{\text{ref}} = 55$ RPM, $b_n = 0.0376$ Nm. Red line: $\Omega_{\text{ref}} = 70$ RPM, $b_n = 0.0500$ Nm (color figure online)

using MATLAB and a fourth-order Runge–Kutta scheme (ode45 function). For this simulation, we also need the moment of inertia of the system which is given by the two disks: 0.0588 kg m^2 .

Following the procedure shown in [12], the system can be linearized around the operational condition and a stability map can be drawn varying Ω_{ref} and b_n ; see Fig. 6. The continuous line separates stability (below the line) and instability (above the line) regions. This serves as a reference for what to expect from the experiment: high speeds tend to stabilize the system and high values of b_n (related to the normal force, and friction coefficient) tend to destabilize the system. However, the challenge of this paper is to build this map experimentally. Next section proposes a strategy to pursue this purpose. The minimum and maximum values of b_n were chosen manually, so that the stability bound falls between the experiments, as shown in Sect. 6.

5 Methodology to experimentally construct stability maps

The construction of torsional stability maps with drill string numerical models has been done by several other authors [12, 34, 36, 38–41]. Nevertheless, even numerically, the impact of initial conditions on it, which might be considerable, has been studied in few works [42]. The challenge faced in this paper is to experimentally construct torsional stability maps for different operational conditions, which has never been attempted before, up to the authors' knowledge. The test rig presents uncertainties, sensitivities, friction, misalignment, oscillations other than torsional, and so

forth. As will be shown in the next section, the transition from stable to unstable dynamics is not deterministic.

In this section, a methodology is proposed to construct stability maps using the test rig. The torsional stability map is constructed varying two operational conditions: axial displacement δ actuated by the stepper motor and the nominal rotational speed Ω_{ref} imposed by the servomotor at the top. The torsional oscillations at the main rotor are analyzed for different values of the pair (Ω_{ref}, δ) . It is expected that higher torsional oscillations occur for low nominal rotational speeds and high normal compressive forces between the main rotor and the friction pins (which is directly related to the platform displacement) [35, 36]. Figure 7 illustrates the main disk without contact with the friction pins. Torsional oscillations and stick–slip are observed in the real drill string system due to a nonlinear bit–rock interaction. The applied nonlinear interaction in the experiment, although different, has a similar effect in creating torsional resistance. As a consequence, it is possible to observe torsional stick–slip in experiments [19], field data [35, 36], and numerical simulations [34].

Previous numerical studies indicate that torsional oscillations change significantly depending on some conditions. For instance, if the contact at the bottom happens before or after the shaft starts rotating [42], and if the transition between rock layers is smooth or abrupt [43].

Since we are interested in the torsional dynamics of the main rotor, its oscillations are evaluated. If the system is unstable, a condition called stick–slip is observed, in which an intermittent sequence of zero speed (stick) is followed

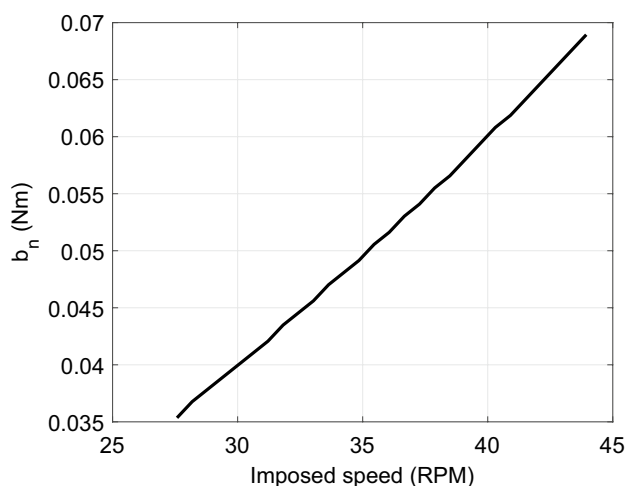


Fig. 6 Stability torsional map obtained for the numerical system (b_n versus the imposed speed). b_n is a parameter related to the axial force and friction coefficient. The continuous line separates stability (below the line) and instability (above the line)



Fig. 7 Main disk and friction pins in test bench

by high speeds. In this condition, the friction torque, due to the contact of the rotor with the pins, is great enough to stop the rotation of the main rotor until the strain energy (accumulated in the shaft) wins and the rotor slips; then, the cycle repeats over and over permanently.

A grid of operational parameters ($\Omega_{\text{ref}}, \delta$) is considered to construct the stability map. Before starting the experiment, the vertical position of the moving parts of the bench is adjusted so that the main rotor is at a nominal distance of 1 mm above the friction pins. This initial lack of contact between the main rotor and the pins before the experiment facilitates zeroing of the load cell. Once this adjustment is made, the test begins, and the moving parts move under the action of the stepper motor and the servomotor according to a previously established sequence of commands. Three different scenarios are implemented to analyze its impact on the torsional stability region:

(Scenario 1) Experimental tests starting the system with friction contact from rest. Initially, the stepper motor is activated, keeping the servomotor at rest, so that the mobile platform moves $x = 1 + \delta$ mm downwards. The 1-mm portion corresponds to the beginning of contact between the main rotor and the friction pins, with zero nominal compression, while the δ portion of the mobile platform movement corresponds to the compression movement of the main rotor over the friction pins. Once this movement is completed, the stepper motor stops moving the mobile platform, and after a few seconds of rest to dampen the vibration in the contact, the servomotor is activated, giving the upper end of the main shaft a nominal rotation speed Ω_{ref} .

(Scenario 2) Experimental tests starting with rotation before the friction contact. In this scenario, the servomotor is activated from the beginning, while the main rotor is at a vertical distance of 1 mm above the friction pins. As soon as the main rotor acquires a permanent movement regime, with nominal rotation equal to that of the servomotor output, the stepper motor is activated, subjecting the mobile platform to a displacement $x = 1 + \delta$ mm downwards, leading the main rotor to the contact with the friction pins, keeping under pressure.

(Scenario 3) Experimental tests imposing axial oscillation of the platform. The main rotor is initially kept at rest. Once frictional contact is established between the main rotor and the friction pins, for a δ displacement of the mobile platform after initiation of contact, the servomotor is driven with a speed Ω_{ref} . At the same time, the stepper motor begins to impose an oscillatory axial movement on the mobile platform around the nominal contact position δ . After some initial tests, the values $f_A = 1$ Hz and $\delta_0 = 0.14$ mm were defined for the axial oscillation frequency and amplitude, respectively.

For each test, the movement of the servomotor ceases after 120s, keeping the two motors at rest for a few

seconds, until the stepper motor is activated again, moving the mobile platform to the original position, that is, so that the main rotor returns to the nominal distance of 1 mm above the friction pins. With that, the test is stopped.

Another important point is related to uncertainties. Each time an experiment is run, its result is a little different (random experiment) due to temperature, point of contact, rubbing surface, etc. Therefore, for each pair ($\Omega_{\text{ref}}, \delta$) five tests are performed. Depending on the dynamical regime, different symbols are plotted in the stability map grid: (i) red “x” means that in the five repeated tests, the stick–slip phenomenon happened permanently, during 120 s; (ii) black “+”: means that in the five repeated tests, the stick–slip phenomenon did not occur at any time, that is, the main rotor did not lock due to dry friction; (iii) green “o”: means either the occurrence of stick–slip at the beginning of the movement, ceasing to happen after a certain moment; or occurrence of stick–slip in at least one test, with non-occurrence in the others, or any other circumstance that does not fit those described for the red “x” or the black “+.”

Two factors observed during the execution of the tests deserve to be highlighted for their influence on the definition of the standard methodology of the tests: the slight inclination of the main rotor about the horizontal plane and the variation in the ambient temperature.

In the construction of the experimental bench, we tried to minimize the inclination of the main rotor as much as possible. Even so, in the already finished prototype, a dependence was observed between the angular position of the main rotor and the normal force during contact with the friction pins. Figure 8a illustrates different compression intensities for 36 variations of 10 degrees, in sequence, in the angular position of the main rotor, for $\delta = 0.5$ mm, completing one revolution. Figure 8b shows the variation in the normal compressive force around the signal window with the highest average intensity. The oscillation of the normal force, observed in Fig. 8b, is mainly due to the lateral movement of the intermediate rotor, since this lateral displacement of the rotor implies a portion of upward movement of the lower end of the main shaft, relieving the weight on the load cell, during contact.

In turn, the variation in the ambient temperature leads to a variation in the length of the main axis. Considering that the standard coefficient of expansion of steel is $\alpha = 1.1 \times 10^{-5} \text{ } ^\circ\text{C}^{-1}$, and that the nominal shaft length is $L = 2500$ mm, the change in shaft length for a variation $\Delta T = 1^\circ\text{C}$ at ambient temperature is given by: $\Delta L = \alpha L \Delta T = (1.1 \times 10^{-5})(2500)(1) = 0.0275$ mm. As a result of this, considering the same initial vertical position set at 1 mm between the main rotor and the friction pins, the downward displacement by $x = 1 + \delta$ mm of the mobile platform, carried out on different days, led to a difference of

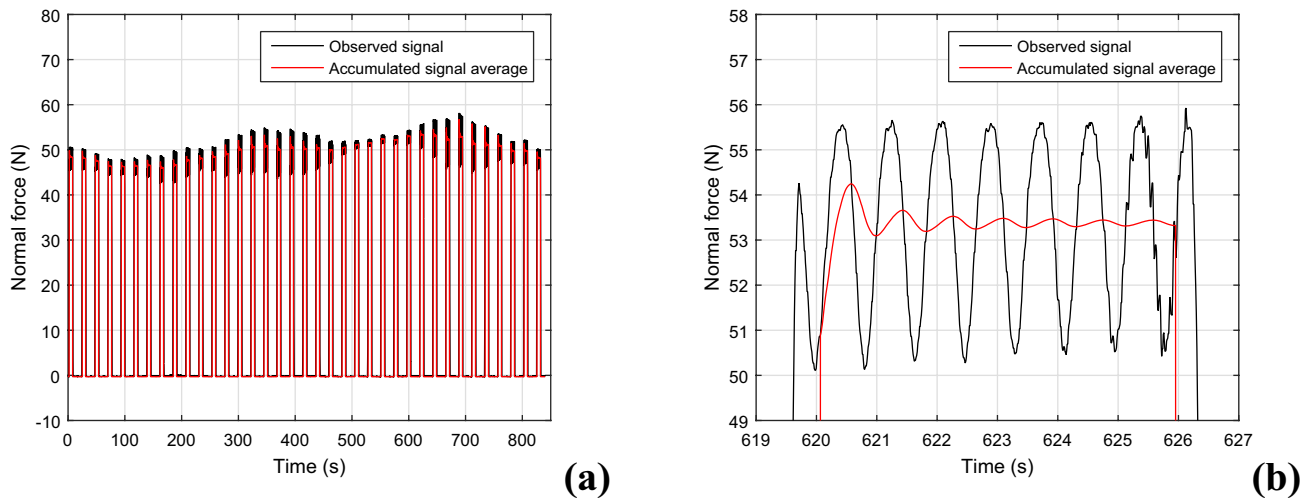


Fig. 8 Time signal of the normal contact force. **a** For different angular positions of the main rotor. **b** Around highest average cumulative compression. Black line: original signal. Red line: accumulated signal average

up to 30 N in the value measured by the cell of load for the compression between the main rotor and the friction pins.

Therefore, for all the tests to be carried out within the same standard condition, before a battery of tests and at different times of the day, the initial vertical position of the main rotor in relation to the friction pins should be adjusted according to the chosen behavior as standard, illustrated in Fig. 8, so that, in the adjusted position, the maximum value of the cumulative average of the normal force for a sequence of 36 angular positions, with a variation of 10 degrees between two subsequent angular positions, and with $\delta = 0.5$ mm, is the same maximum value of the cumulative average of the normal force as shown in Fig. 8, that is, 53.4 N.

6 Experimental stability maps

For scenario 1, Fig. 9a shows the stability map, based on the first tests performed, considering on the abscissa axis different nominal rotational speeds Ω_{ref} and on the ordinate axis the values of the δ displacement of the mobile platform. The first battery of experiments, summarized in Fig. 9a–c, was carried out between March 29, 2023, and May 17, 2023.

Figure 9(a) shows that instability (high torsional oscillations), represented by the red “x,” occurs for low Ω_{ref} and high δ (related to the normal force between the main rotor and the friction pins), by previous investigations [35, 36]. The green zone corresponds to a transition zone between operating regimes with stick–slip (red zone) and without stick–slip (black zone).

Figure 9(b) shows the stability map generated from the second scenario, where the experimental tests start with rotation. The transition zone of the first tests is used as a

reference (dashed black lines). The new transition zone is represented by the blue dashed line.

From the results obtained, it can be concluded that, for a displacement $\delta = 0.3$ mm, the black zone advances over the green zone until it includes the speed $\Omega_{\text{ref}} = 10$ RPM, not having been observed the same for the other levels of compression in the frictional contact. This result is relevant, considering that a simple change in procedure already implies a small reduction in the occurrence of stick–slip.

Figure 9(c) shows the stability map from the third battery of tests, where an axial oscillation is imposed to the platform. Again, the transition zone of the first tests is used as a reference (dashed black lines). The new transition zone is represented by the blue dashed line. Figure 10 shows the displacement imposed on the mobile platform, in relation to the imminent position of frictional contact, for $\delta = 0.5$ mm, $f_A = 1$ Hz and $\delta_0 = 0.14$ mm. Due to the stepper motor’s response time limitations, after some initial tests, the values $f_A = 1$ Hz and $\delta_0 = 0.14$ mm were set for the frequency and amplitude of the axial oscillation, respectively. The frequency of 1 Hz was chosen as a first attempt for excitation, with the sole criterion of not coinciding with any of the initial natural frequencies of the test rig, and the amplitude 0.14 mm was selected as the maximum possible oscillation amplitude at this frequency, taking into account the limitations of the experimental apparatus.

Comparing Fig. 9a with Fig. 9b, it is possible to notice an increase in the stable area (blue and black markers) over the transition zone (green markers) for $\delta = 0.5$ mm and $\delta = 0.6$ mm, until the speeds $\Omega_{\text{ref}} = 27.5$ RPM and $\Omega_{\text{ref}} = 32.5$ RPM are included, respectively. The green zone also advanced over the red zone for $\delta = 0.6$ mm, also encompassing speed $\Omega_{\text{ref}} = 15$ RPM.

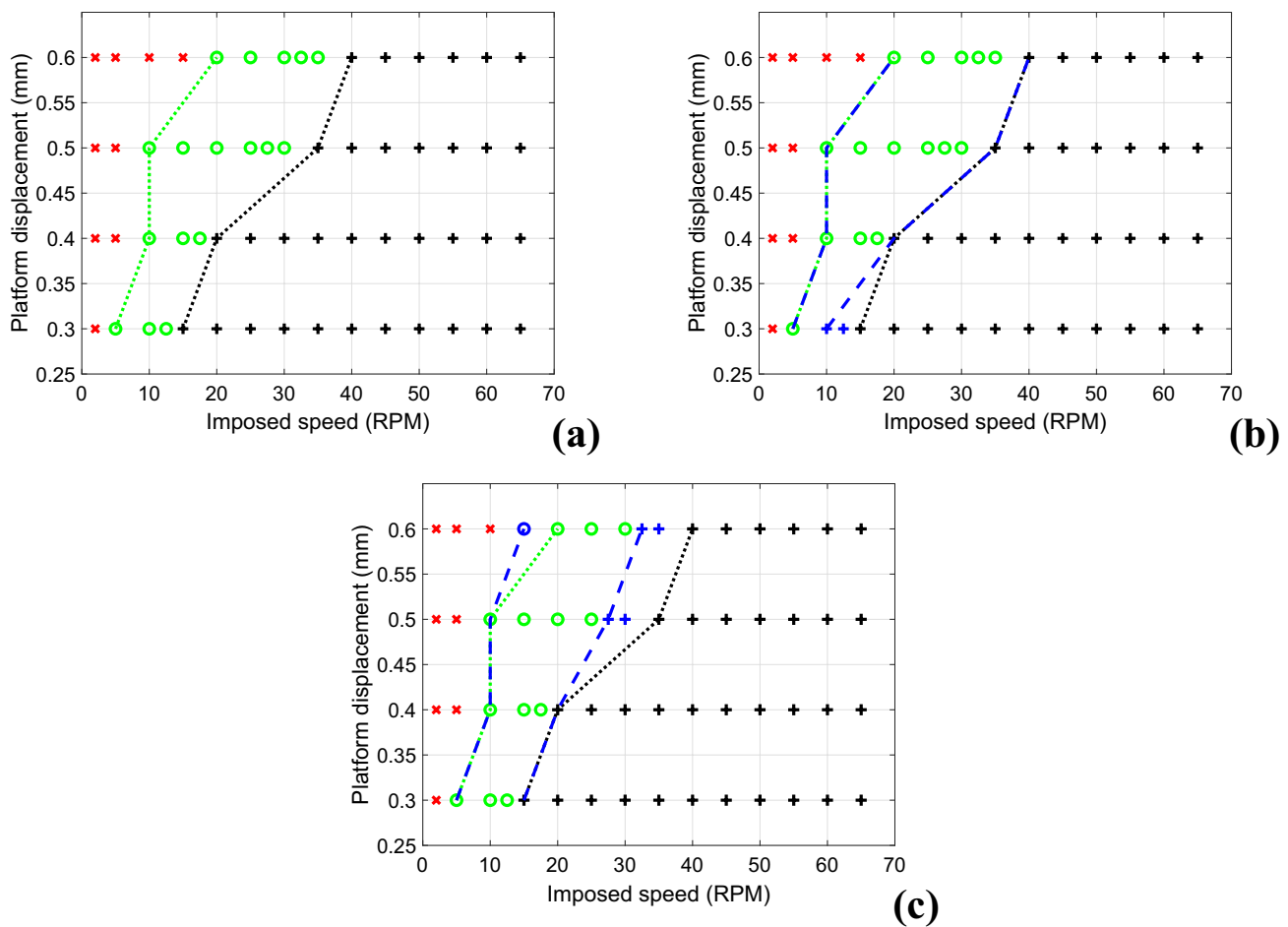


Fig. 9 Torsional stability map (platform displacement versus imposed speed). **a** Experimental tests starting the system with friction contact from rest. **b** Experimental tests starting with rotation before the friction contact. **c** Experimental tests imposing axial oscillation of the platform. Black crosses represent stable responses, red marks represent

unstable responses (high torsional oscillations), and green circles represent transition zone type 1. Dashed green and black lines delimit the transition zone of the experimental tests starting from rest. The blue dashed lines delimit the transition zone for the other two scenarios (b) and (c) (color figure online)

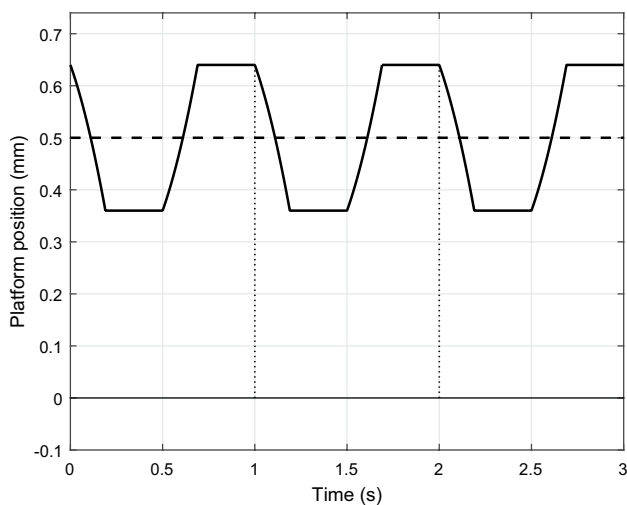


Fig. 10 Platform displacement time signal for $\delta = 0.5$ mm, $f_A = 1$ Hz, and $\delta_0 = 0.14$ mm

To evaluate the repeatability of results under the same predefined methodology, the experimental tests were repeated later, between May 25, 2023, and June 13, 2023, considering the same three conditions of the previous tests: (i) starting from rest, (ii) starting with rotation, and (iii) inclusion of oscillatory axial movement of the mobile platform. Tests under intermediate nominal compression displacements were included. Figure 11 summarizes the new results obtained.

The two sets of experiments demonstrate that the stability zone shows a significant reduction in the second set of tests. Not controllable factors, such as ambient temperature fluctuations, humidity, and wear on rig components, change the frictional contact and, consequently, the torsional dynamic stability. However, it can be stated that making frictional contact with the rotor in motion or imposing a longitudinal oscillation at the top of the shaft in both test sets resulted in an increase in the stability zone.

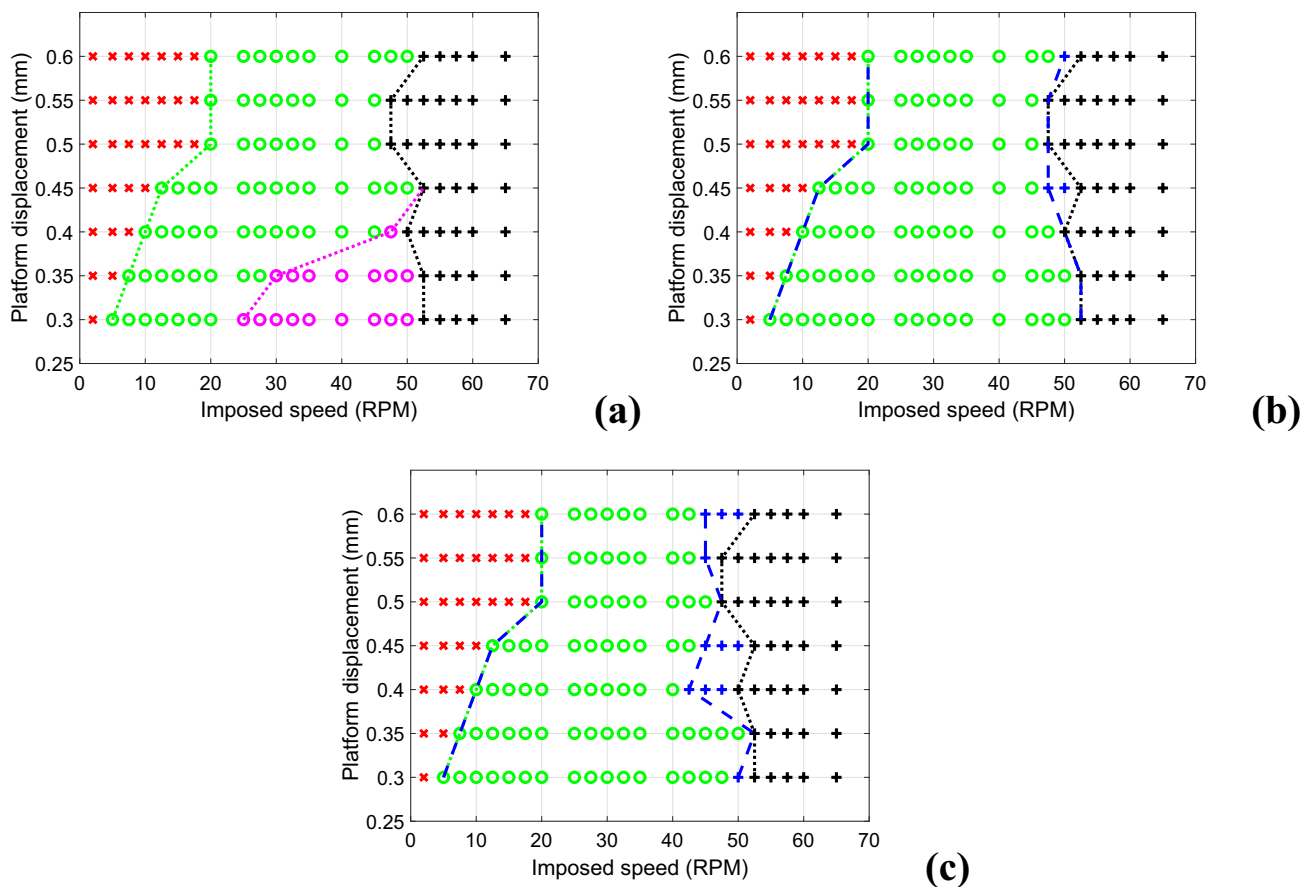


Fig. 11 Torsional stability map (platform displacement versus imposed speed). **a** Experimental tests starting the system with friction contact from rest. **b** Experimental tests starting with rotation before the friction contact. **c** Experimental tests imposing axial oscillation of the platform. Black crosses represent stable responses, red marks represent unstable responses (high torsional oscillations), green cir-

cles represent transition zone type 1, and lilac circles represent transition zone type 2. Dashed green and black lines delimit the transition zone of the experimental tests starting from rest. The blue dashed lines delimit the transition zone for the other two scenarios (b) and (c) (color figure online)

In Fig. 11a, the lilac circles correspond to the area of the transition zone with a new dynamic behavior, denominated in this article as transition zone type 2. In turn, the green circles correspond to the so-called transition zone type 1. The time signal of the rotational speed of the main rotor will be depicted in the next section. The transition zone type 2 is evidenced only in Fig. 11a.

Comparing the tests carried out in different periods between March and June, it is noted that the red zone has undergone some changes. In the second tests, the unstable (red) region and the transition zone enlarged, more prominently at low compression. This change is attributed to the influence of the difference in ambient temperature and material wear between the two periods of execution of the experiments. In any case, there is an advance in the useful zone—blue zone in Figs. 9b, c, 11b, c—either when making frictional contact with the rotor already in motion, or adding axial oscillation to the movement of the mobile platform during frictional contact.

Understanding the consequences of changing the operational condition in a slender shaft with nonlinear interaction might inspire new strategies to be implemented in the field to avoid torsional oscillations and improve the efficiency of drilling.

Finally, it is possible to compare qualitatively the stability bounds of the numerical model, Fig. 6, and the two sets of experimental responses, Figs. 9a, 11a. Figure 12 shows the three curves together, where the numerical response (continuous line) normalizes the values of b_n between 0.03 and 0.06. Note that there is a very good consistency between the experimental and numerical results, even though a simple model is considered. These results might guide further developments on deterministic and stochastic dynamic models.

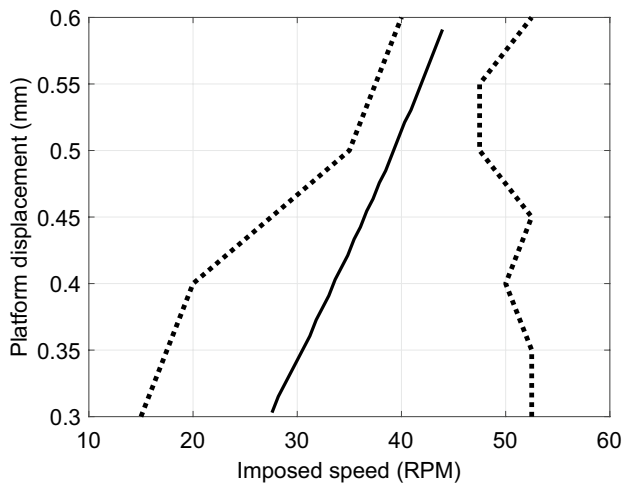


Fig. 12 Stability torsional map (platform displacement versus imposed speed) obtained for the numerical model (continuous line taken from Fig. 6) and experimental maps, which were taken from the two sets of experiments, dashed black lines of Figs. 9a and 11a

7 Concluding remarks

A new test rig aiming at analyzing drill string dynamics was presented. A novel methodology was proposed to construct an experimental torsional stability map. Results show that starting with shaft rotation before the axial contact and applying axial oscillations during contact improves torsional stability. In addition, temperature and material wear have a great influence on the stability map.

The conditions considered in the experiment might happen in the real drill string. It seems that proposing a controlled axial displacement might increase the stable region. It is difficult to assess the effect of oscillations at the top of the drill string on bit bounce vibrations in the drill string based on the experimental data from this test rig, as the longitudinal frequencies of the rig are high and undetectable by the sensors used. However, it is expected that inducing low-frequency longitudinal vibrations at the top of the drill string would have little influence on bit bounce vibrations, as the former are of a much lower order of magnitude.

The experimental data produced in this article may guide new developments, for instance, other experimental strategies to build a stability map and strategies for vibration control. In addition, a more complete numerical model can be considered (finite element, etc.), and uncertainties quantification strategies pursued.

Finally, the presented test bench will be explored in different ways, such as analyzing lateral vibrations, lateral impact/rubbing, and coupled torsional–axial–lateral dynamics.

Acknowledgements The first author would like to thank the Graduate Program in Mechanical Engineering at USP, for supporting my

technical training, and also to CAPES, for the financial support scholarship. The last author would like to acknowledge that this investigation was financed in part by the Brazilian agencies: CAPES—Grant PROEX 2024, CNPQ—Grant 302378/2022-7, and FAPERJ—Grant E-26/201.183/2022.

Author contributions These authors contributed equally to this work.

Funding This investigation was financed in part by the Brazilian agencies: CAPES, CNPQ, and FAPERJ.

Data availability Experiments results are made available under the GitHub repository PhD-USP-AD <https://github.com/AdrianoDomeny/PhD-USP-AD>.

Declarations

Conflict of interest The authors have no conflict of interest as defined by Springer, or other interests that might be perceived to influence the results and/or discussion reported in this paper.

Ethical approval Not applicable.

References

- Ritto TG, Soize C, Sampaio R (2009) Non-linear dynamics of a drill-string with uncertain model of the bit-rock interaction. *Int J Non-Linear Mech* 44(8):865–876. <https://doi.org/10.1016/j.ijnonlinmec.2009.06.003>
- Tran Q-T, Nguyen K-L, Manin L, Andrianoely M-A, Dufour R, Mahjoub M, Menand S (2019) Nonlinear dynamics of directional drilling with fluid and borehole interactions. *J Sound Vib*. <https://doi.org/10.1016/j.jsv.2019.114924>
- de Moraes LPP, Savi MA (2019) Drill-string vibration analysis considering an axial-torsional-lateral nonsmooth model. *J Sound Vib* 438:220–237. <https://doi.org/10.1016/j.jsv.2018.08.054>
- Goicoechea HE, Lima R, Buezas FS, Sampaio R (2024) A comprehensive cosserat rod drill-string model for arbitrary well geometry that includes the dynamics of the cutting and lateral contact. *J Sound Vib*. <https://doi.org/10.1016/j.jsv.2023.118035>
- Tang F, Liu Y, Xia J, Yang S, Lv J (2025) Nonlinear rub-impact characteristics of drillstring-wellbore and wear quantitative evaluation method. *Geoenergy Sci Eng*. <https://doi.org/10.1016/j.geoen.2024.213466>
- Silva RS, Ritto TG, Savi MA (2021) Shape memory alloy couplers applied for torsional vibration attenuation of drill-string systems. *J Pet Sci Eng*. <https://doi.org/10.1016/j.petrol.2021.108546>
- Lobo DM, Ritto TG, Castello DA, Batou A (2022) On the stochastic bit-rock interaction disturbances and its effects on the performance of two commercial control strategies used in drill strings. *Mech Syst Signal Process*. <https://doi.org/10.1016/j.ymssp.2021.108229>
- Cruz Neto HJ, Trindade MA (2023) Control of drill string torsional vibrations using optimal static output feedback. *Control Eng Pract*. <https://doi.org/10.1016/j.conengprac.2022.105366>
- Barjini AH, Khoshnazar M, Moradi H (2024) Design of a sliding mode controller for suppressing coupled axial & torsional vibrations in horizontal drill strings using extended kalman filter. *J Sound Vib*. <https://doi.org/10.1016/j.jsv.2024.118477>
- Caballero EF, Lobo DM, Di Vaio MV, Silva ECCM, Ritto TG (2021) Support vector machines applied to torsional vibration severity in drill strings. *J Braz Soc Mech Sci Eng*. <https://doi.org/10.1007/s40430-021-03089-z>

11. Khoshroo M, Eftekhari M (2022) Probabilistic analysis of drill string under uncertain conditions for flow velocity and axial compressive load. *Appl Ocean Res*. <https://doi.org/10.1016/j.apor.2022.103142>
12. Castello DA, Ritto TG (2023) ABC for model selection and parameter estimation of drill-string bit-rock interaction models and stochastic stability. *J Sound Vib*. <https://doi.org/10.1016/j.jsv.2022.117537>
13. Liu X, Vljajic N, Long X, Meng G, Balachandran B (2013) Nonlinear motions of a flexible rotor with a drill bit: Stick-slip and delay effects. *Nonlinear Dyn* 72(1–2):61–77. <https://doi.org/10.1007/s11071-012-0690-x>
14. van de Wouw N, Monsieurs FHA, Detournay E (2016) Dynamic state-feedback control of nonlinear three-dimensional directional drilling systems 49:85–90. <https://doi.org/10.1016/j.ifacol.2016.10.144>
15. Patil PA, Teodoru C (2013) A comparative review of modelling and controlling torsional vibrations and experimentation using laboratory setups. *J Petrol Sci Eng* 112:227–238. <https://doi.org/10.1016/j.petrol.2013.11.008>
16. Srivastava S, Teodoru C (2019) An extensive review of laboratory scaled experimental setups for studying drill string vibrations and the way forward. *J Pet Sci Eng*. <https://doi.org/10.1016/j.petrol.2019.106272>
17. Liao C-M, Balachandran B, Karkoub M, Abdel-Magid YL (2011) Drill-string dynamics: Reduced-order models and experimental studies. *J Vib Acoust Trans ASME* 10(1115/1):4003406
18. Mihajlovic N, Van De Wouw N, Hendriks MPM, Nijmeijer H (2006) Friction-induced limit cycling in flexible rotor systems: an experimental drill-string set-up. *Nonlinear Dyn* 46(3):273–291. <https://doi.org/10.1007/s11071-006-9042-z>
19. Cayres B, da Fonseca C, Santos A, Weber HI (2015) Analysis of Dry Friction-induced Stick-slip in an Experimental Test Rig Modeling a Drill String 21:195–204. https://doi.org/10.1007/978-3-319-06590-8_16
20. Real FF, Lobo DM, Ritto TG, Pinto FANC (2018) Experimental analysis of stick-slip in drilling dynamics in a laboratory test-rig. *J Petrol Sci Eng* 170:755–762. <https://doi.org/10.1016/j.petrol.2018.07.008>
21. Real FF, Batou A, Ritto TG, Desceliers C (2019) Stochastic modeling for hysteretic bit-rock interaction of a drill string under torsional vibrations. *JVC/J Vib Control* 25(10):1663–1672. <https://doi.org/10.1177/1077546319828245>
22. Kapitaniak M, Vaziri Hamaneh V, Chávez JP, Nandakumar K, Wiercigroch M (2015) Unveiling complexity of drill-string vibrations: experiments and modelling. *Int J Mech Sci* 101–102:324–337. <https://doi.org/10.1016/j.ijmecsci.2015.07.008>
23. Tian J, Wei L, Yang L, Dai L, Zhang T, Liu H (2020) Research and experimental analysis of drill string dynamics characteristics and stick-slip reduction mechanism. *J Mech Sci Technol* 34(3):977–986. <https://doi.org/10.1007/s12206-020-0201-9>
24. Tian J, Tang L, Yang Y, Dai L, Xiong C (2022) Drill string dynamics and experimental study of constant torque and stick-slip reduction drilling tool. *Pet Sci Technol*. <https://doi.org/10.1080/10916466.2022.2120008>
25. Tian J, Tang L, Yan B, Song H, Mao L (2023) Dynamic characteristics and experimental research of dual-piston axial oscillation drag reduction tool. *J Energy Resour Technol Trans ASME*. <https://doi.org/10.1115/1.4056114>
26. Yu F, Huang G, Li W, Ni H, Huang B, Li J, Duan J (2023) Modeling lateral vibration of bottom hole assembly using cosserat theory and laboratory experiment verification. *Geoenergy Sci Eng* 222:211359
27. Pires I, Ayala HVH, Weber HI (2023) Nonlinear ensemble gray and black-box system identification of friction induced vibrations in slender rotating structures. *Mech Syst Signal Process*. <https://doi.org/10.1016/j.ymssp.2022.109815>
28. dos Santos AD, de Toledo Fleury A (2024) Control of a slender rotary system subjected to dry friction and rub. *J Braz Soc Mech Sci Eng* 46(5):320. <https://doi.org/10.1007/s40430-024-04914-x>
29. Domeny A (2023) Dynamics and control of a slender flexible rotating structure subject to torsion and rubbing (in portuguese). PhD thesis, Universidade de São Paulo. <https://www.teses.usp.br/>
30. Domeny A (2015) Dynamic behavior of a slender rotating shaft subject to stick-slip action in two distinct regions (in portuguese). Master's thesis, PUC-Rio. <https://www.maxwell.vrac.puc-rio.br/26272/26272.PDF>
31. dos Santos A.D, de Toledo Fleury A (2017) Sliding mode control of a flexible rotating system subject to concentrated dry friction. 24th ABCM International Congress of Mechanical Engineering - COBEM
32. dos Santos A.D, de Toledo Fleury A (2019) Sliding mode control strategies for flexible rotating systems. 19th International Symposium on Dynamic Problems of Mechanics - DINAME
33. Westermann H, Gorelik I, Rudat J, Moritz C, Neubauer M, Wallaschek J, Höhn O (2015) A new test rig for experimental studies of drillstring vibrations. *SPE Drill Complet* 30(2):119–128. <https://doi.org/10.2118/176019-PA>
34. Ritto TG, Ghandchi-Tehrani M (2019) Active control of stick-slip torsional vibrations in drill-strings. *JVC/J Vib Control* 25(1):194–202. <https://doi.org/10.1177/1077546318774240>
35. Pavone D.R, Desplans J.P (1994) Application of High Sampling Rate Downhole Measurements for Analysis and Cure of Stick-slip in Drilling, vol. Delta, pp. 335–345. <https://doi.org/10.2118/28324-ms>
36. Ritto TG, Aguiar RR, Hbaieb S (2017) Validation of a drill string dynamical model and torsional stability. *Meccanica* 52(11–12):2959–2967. <https://doi.org/10.1007/s11012-017-0628-y>
37. Tucker R.W, Wang C (1997) The excitation and control of torsional slip-stick in the presence of axial vibrations. <http://www.lancs.ac.uk/users/spc/physics.htm>
38. Nogueira BF, Ritto TG (2018) Stochastic torsional stability of an oil drill-string. *Meccanica* 53(11–12):3047–3060. <https://doi.org/10.1007/s11012-018-0859-6>
39. Zhang H, Detournay E (2022) A high-dimensional model to study the self-excited oscillations of rotary drilling systems. *Commun Nonlinear Sci Numer Simul*. <https://doi.org/10.1016/j.cnsns.2022.106549>
40. Liu X, Meng G, Balachandran B (2023) Drill-string stability and stress localization: influence of complex delay effects and dry friction. *Int J Non Linear Mecha*. <https://doi.org/10.1016/j.ijnonlinmec.2023.104559>
41. Faghihi MA, Mohammadi H, Yazdi EA, Egtesad M, Tashakori S (2024) Distributed model for the drill-string system with multiple regenerative effects in the bit-rock interaction. *J Sound Vib*. <https://doi.org/10.1016/j.jsv.2023.118120>
42. Cunha-Lima L.C, Aguiar R.R, Ritto T.G, Hbaieb S (2015) Analysis of the torsional stability of a simplified drillstring. In: 17th International Symposium on Dynamic Problems of Mechanics - DINAME
43. Lobo DM, Ritto TG, Castello DA (2017) Stochastic analysis of torsional drill-string vibrations considering the passage from a soft to a harder rock layer. *J Braz Soc Mech Sci Eng* 39(6):2341–2349. <https://doi.org/10.1007/s40430-017-0800-2>

Publisher's Note Springer Nature remains neutral with regard to jurisdictional claims in published maps and institutional affiliations.

Springer Nature or its licensor (e.g. a society or other partner) holds exclusive rights to this article under a publishing agreement with the author(s) or other rightsholder(s); author self-archiving of the accepted manuscript version of this article is solely governed by the terms of such publishing agreement and applicable law.